Available online at www.sciencedirect.com
ScienceDirect
Journal of Power Sources 175 (2008) 276–287
JOURNAL OF POWER SOURCES
www.elsevier.com/locate/jpowsour

Two-dimensional two-phase thermal model for passive direct methanol fuel cells

R. Chen, T.S. Zhao *, W.W. Yang, C. Xu

Department of Mechanical Engineering, The Hong Kong University of Science and Technology, Clear Water Bay, Kowloon, Hong Kong SAR, China

Received 10 August 2007; received in revised form 26 September 2007; accepted 26 September 2007
Available online 2 October 2007

Abstract

A two-dimensional two-phase thermal model is presented for direct methanol fuel cells (DMFC), in which the fuel and oxidant are fed in a passive manner. The inherently coupled heat and mass transport, along with the electrochemical reactions occurring in the passive DMFC is modeled based on the unsaturated flow theory in porous media. The model is solved numerically using a home-written computer code to investigate the effects of various operating and geometric design parameters, including methanol concentration as well as the open ratio and channel and rib width of the current collectors, on cell performance. The numerical results show that the cell performance increases with increasing methanol concentration from 1.0 to 4.0 M, due primarily to the increased operating temperature resulting from the exothermic reaction between the permeated methanol and oxygen on the cathode and the increased mass transfer rate of methanol. It is also shown that the cell performance upgrades with increasing the open ratio and with decreasing the rib width as the result of the increased mass transfer rate on both the anode and cathode.
© 2007 Elsevier B.V. All rights reserved.

Keywords: Fuel cell; Passive DMFC; Two-phase flow; Heat and mass transfer; Thermal management

1. Introduction

The direct methanol fuel cell (DMFC) has been widely investigated as an alternative power source for powering various potable electronic devices because they can offer the promises of higher energy efficiency and higher energy density. Over the past decades, extensive efforts have been focused on the active-feed DMFC with the fuel fed by a liquid pump and oxidant fed by a gas compressor [1–3]. Nevertheless, these ancillary devices not only make the fuel cell system complex but also lower the power density because of the parasitic losses. For this reason, the passive DMFC with neither liquid pumps nor gas compressors has been proposed and studied [4–12]. This type of passively operated fuel cell is appealing because it not only offers the advantage of a simpler and more compact system, but also eliminates the parasitic power losses for powering the ancillary devices required in the active DMFCs. However, compared to its counterpart—the active DMFC, the performance of the passive DMFC is lower because of the inability to handle the excess liquid water on the cathode and too much heat loss from the fuel cell to the ambient, resulting in a lower cell operating temperature. Hence, the added attention has to be given to the thermal and water management for the passive DMFC.

In the DMFC, the intrinsically coupled physicochemical processes simultaneously occur, including heat and mass transfer, electrochemical reactions, ionic and electronic transfer. Since it is difficult to experimentally quantify the interrelated parameters governing the DMFC, numerical modeling becomes essential for the optimization of the cell design and operating conditions. A number of studies [13–34] have been reported on simulation of both PEMFCs and DMFCs. Most previous models were developed based on the single-phase flow theory [13–26], which include semi-empirical model [13] and one-dimensional and multi-dimensional models [17–25]. However, since the single-phase model cannot objectively reflect the two-phase mass transport process occurring in the DMFC, as revealed by the visualization study [3], the two-phase models for the DMFC have recently been reported [27–35]. Murgia et al. [27] developed a one-dimensional, two-phase, multi-component steady-state model based on the phenomenological transport

* Corresponding author. Tel.: +852 2358 8647; fax: +852 2358 1543.
E-mail address: metzhao@ust.hk (T.S. Zhao).

0378-7753/$ – see front matter © 2007 Elsevier B.V. All rights reserved.
doi:10.1016/j.jpowsour.2007.09.086

Nomenclature

c_j	specific heat capacity of species j ($J\,mol^{-1}\,K^{-1}$)
C_j	concentration of species j ($mol\,m^{-3}$)
D_j	diffusivity of species j ($m^2\,s^{-1}$)
E	thermodynamic equilibrium potential (V)
F	Faraday's constant ($C\,mol^{-1}$)
G	Gibbs free energy ($J\,mol^{-1}$)
h	heat transfer coefficient ($W\,m^{-2}$)
h_v	evaporation heat of water ($J\,mol^{-1}$)
H	enthalpy ($J\,mol^{-1}$)
i	local current density ($A\,m^{-2}$)
i_p	parasitic current density resulting from methanol crossover ($A\,m^{-2}$)
i^{ref}	exchange current density ($A\,m^{-2}$)
I	cell current density ($A\,m^{-2}$)
k_{rg}	relative permeability of gas phase
k_{rl}	relative permeability of liquid phase
k_c	condensation rate constant ($1\,s^{-1}$)
k_v	evaporation rate constant ($1\,atm^{-1}\,s^{-1}$)
K	permeability (m^2)
l	channel and rib width (m)
M_j	molecular weight of species j ($kg\,mol^{-1}$)
n_{H_2O}	electro-osmotic drag coefficient of water
n_d^m	electro-osmotic drag coefficient of methanol
N_j	molar flux of species j ($mol\,m^{-2}\,s^{-1}$)
P	atmosphere pressure (Pa)
P_c	pressure (Pa)
P_g	gas pressure (Pa)
P_l	liquid pressure (Pa)
q	heat generation rate ($W\,m^{-2}$)
R	interfacial transfer rate or gas constant ($mol\,m^{-3}\,s^{-1}$ or $J\,mol^{-1}\,K^{-1}$)
$R_{contact}$	contact resistance ($\Omega\,m^2$)
s	liquid saturation in porous media
T	temperature (K)
$\mathbf{u}$	superficial velocity vector ($m\,s^{-1}$)
V	potential (V)
x	coordinate
y	coordinate or mole fraction
Y^*	dimensionless coordinate

Greek letters

α_a	charge transfer coefficient at anode
α_c	charge transfer coefficient at cathode
δ	thickness of the membrane (m)
η	overpotential (V)
θ_c	contact angle (°)
κ	ionic conductivity of membrane ($1\,\Omega^{-1}\,m^{-1}$)
μ	viscosity ($kg\,m^{-1}\,s^{-1}$)
ρ	density ($kg\,m^{-3}$)
σ	surface tension ($N\,m^{-1}$)

Superscripts and subscripts

a	anode
acl	anode catalyst layer
agdl	anode gas diffusion layer
c	cathode
cell	cell
ccl	cathode catalyst layer
cgdl	cathode gas diffusion layer
ccc	cathode current collector
eff	effect value
g	gas phase
H_2O	water
l	liquid phase
m	methanol
mem	polymer electrolyte membrane
O_2	oxygen
ref	reference value
sat	saturated
v	vapor

equations. This model introduced a Gaussian function to approximately account for the influence of the capillary pressure on the effective gas porosity. Wang and Wang [28] developed a model for the DMFC based on the mixture multi-phase flow model. Divisek et al. [30] presented a two-dimensional, two-phase model for the DMFC with the computational domain of a cross-section perpendicular to the flow direction at a certain position, and the model was restricted to the porous electrodes and membrane of the cell. In their work, the presence of hydrophilic and hydrophobic pores was taken into account by introducing a supposed relationship between capillary pressure and saturation which is different from the Levereete function as used in [28]. In addition, the two-phase mass transport phenomena in PEMFCs have been modeled based on the unsaturated flow theory in porous media (UFT) [31–34].

In addition to modeling of active DMFCs and PEMFCs mentioned above, the mathematical models for the air-breathing PEMFCs and passive DMFCs have also been reported [36–48]. Ziegler et al. [42] developed a single-phase two-dimensional non-isothermal model for an air-breathing PEMFC and investigated the effect of the geometric design of the cathode end plate on the gas, potential and cell temperature distribution. Hwang [44] presented a three-dimensional model to study the species transport and electrochemical characteristics in a free-breathing cathode of a planar fuel cell, in which the Brinkman extension to the Darcy's law was employed to describe the gas-mixture flow in the porous cathode. The effects of breathing-hole arrangements and open-area ratio of the current collector on the electrochemical performance were also examined. Recently, Rice and Faghri [48] developed a transient two-dimensional, multi-phase, multi-component model for the DMFC with a passive fuel delivery system. The passive delivery system utilized a porous medium to passively deliver methanol to the fuel cell while controlling the concentration

of methanol at the anode side to limit the amount of methanol crossover.

Our literature review indicates that the two-dimensional two-phase model with the heat transfer effect for the passive DMFC has not been reported yet. However, as mentioned above, the thermal and water management is crucial for the passive DMFC. Hence, the two-phase transport in the passive DMFC with taking account of the heat transfer effect is essential for better understanding of transport phenomena in this type of fuel cell. In this work, we developed a two-dimensional two-phase thermal model for the passive DMFC. The two-phase transport in the anode and cathode porous region (gas diffusion layer) is formulated based on the unsaturated flow theory in porous media. With this model, the effects of species distribution, current density distribution and temperature distribution as well as the effects of the various operating and geometric design parameters on the cell performance are studied.

2. Mathematical model

Consider the passive DMFC sketched in Fig. 1a, which consists a fuel tank, an anode current collector (ACC), an anode gas diffusion layer (AGDL), an anode catalyst layer (ACL), a polymer electrolyte membrane (MEM), a cathode catalyst layer (CCL), a cathode gas diffusion layer (CGDL), and a cathode current collector (CCC). On the anode, methanol is transported from the fuel tank to the ACL, where part of methanol is electrochemically oxidized to form CO_2, while the remainder permeates the membrane and reacts with oxygen on the cathode. The produced gas CO_2 transfers back to the fuel tank and is emitted to the ambient. On the cathode, oxygen is passively taken from the ambient air to the CCL, where it is reduced to form water and heat. The generated water moves out through the CGDL by the capillary force. The heat generated in the fuel cell is lost from the CCC to the ambient by natural convection.

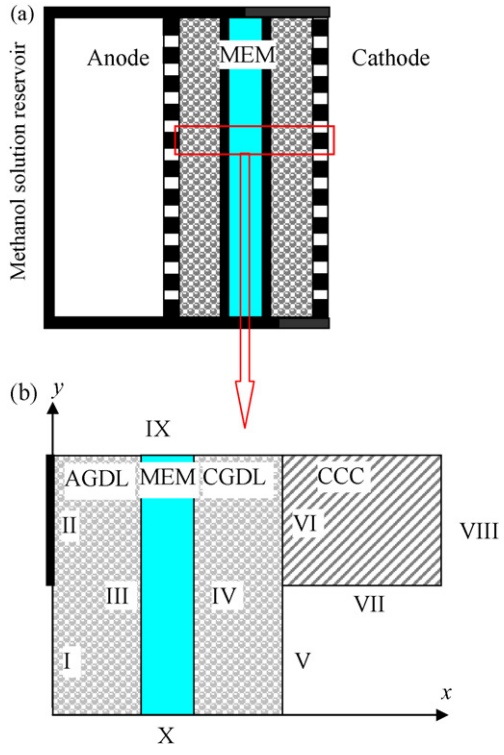

Fig. 1. (a) Schematic of the passive DMFC; (b) the computation domain.

To save the computational expense, a unit region, as illustrated in Fig. 1b, can be taken from the entire cell as the computational domain, in which the components in the horizontal direction remain the same as in Fig. 1a, but in the vertical direction only the half channel and half rib width are included because of the lateral symmetry with respect to the middle point of channel width. Note that the x-axis and y-axis origins are set at the outer surface of the AGDL and at the middle of channel width, respectively. For convenience of description, each boundary and interface are designated with Roman numerals from I to X. The model is formulated based on the following general simplifications and assumptions:

(1) The fuel cell is assumed to operate under steady-state conditions.
(2) The methanol concentration in the fuel tank remains constant during the fuel cell discharging.
(3) The fuel tank, ACC, and AGDL are well insulated from the ambient. No heat is lost from these components to the ambient. Thus, the temperature at each of these components is the same as that at ACL.
(4) Considering that ACL and CCL are much thinner than AGDL, CGDL and MEM, they are treated as an interface and the temperature and concentration distributions are uniform.
(5) On the cathode, the heat is transferred from the CCC to the ambient by natural convection.
(6) Since the reaction rate of methanol on the cathode is rather fast, the methanol in the CCL is assumed to be completely depleted.
(7) Since the variation in the fluid viscosity and density with temperature is relatively small in the calculated range, these properties are considered to be constant.
(8) Considering only CO_2 in the anode gas phase, the methanol vapor and water vapor transport is ignored.

2.1. Two-phase mass transport in the AGDL

We first consider the two-phase mass transport in the AGDL. Based on unsaturated flow theory in porous media, on the anode, the liquid pressure is assumed to be constant. Thus, the transfer of methanol from the fuel tank to the ACL relies on diffusion only, where part of methanol is electrochemically oxidized to produce gas CO_2, electrons and protons, while the remainder permeates the membrane and arrives in the CCL. The produced gas CO_2 transfers back to the fuel tank by the capillary force. This two-phase counter-flow mass transport in the AGDL can be modeled by:

$$\nabla \cdot (D_{\mathrm{m}}^{\mathrm{eff}} \nabla C_{\mathrm{m}}^{\mathrm{agdl}}) = 0 \quad \text{(liquid phase)}, \tag{1}$$

and

$$\nabla \cdot \left(\frac{\rho_g}{M_g} \mathbf{u}_g \right) = 0 \quad \text{(gas phase)}, \tag{2}$$

where D_m^{eff}, ρ_g and M_g represent the effective diffusivity of methanol in the AGDL, the density and molar weight of gas CO_2, respectively. In Eq. (2), $\mathbf{u}_g$ is the superficial velocity vector based on the total cross-sectional area of fluids and porous medium, which can be obtained from Darcy's law:

$$\mathbf{u}_g = -\frac{K k_{rg}}{\mu_g} \nabla p_g \tag{3}$$

with K, k_{rg} and μ_g denoting the absolute permeability of the AGDL, the relative permeability of the gas phase and the viscosity of the gas phase, respectively. The pressure difference between the gas phase and liquid phase is related to the capillary pressure:

$$p_c = p_g - p_l = \sigma \cos(\theta_c) \left(\frac{\varepsilon}{K} \right)^{0.5} J(s), \tag{4}$$

where $J(s)$ represents the Levertte function with s being as liquid saturation in a porous medium (see Table 1). Based on the assumption of the constant liquid pressure in the AGDL, we combine Eqs. (2)–(4) to obtain:

$$\nabla \cdot \left(\frac{\rho_g}{M_g} \frac{K k_{rg}}{\mu_g} \sigma \cos(\theta_c) \left(\frac{\varepsilon}{K} \right)^{0.5} \nabla J(s) \right) = 0. \tag{5}$$

2.2. Two-phase mass transport in the CGDL

We now turn our attention to the two-phase mass transport in the cathode gas diffusion layer (CGDL). Oxygen transfers to the cathode catalyst layer (CCL), where part of the oxygen is electrochemically reduced to form liquid water, while the remainder directly reacts with the permeated methanol to produce heat and liquid water and CO_2. The liquid water generated in the CCL and that permeated from the anode move to the ambient by the capillary force. It should be noted that this process is coupled with the liquid water evaporation. Assuming that the pressure of gas phase is constant, we can treat this mass transport process in the gas phase to be a diffusion problem. As a result, this two-phase counter-flow mass transport in the CGDL can be modeled with the following equations:

$$-\nabla \cdot (-D_{O_2}^{eff} \nabla C_{O_2}^{cgdl}) = 0 \quad \text{(gas phase)}, \tag{6}$$

$$-\nabla \cdot (-D_v^{eff} \nabla C_v^{cgdl}) - R_w = 0 \quad \text{(gas phase)}, \tag{7}$$

and

$$-\nabla \cdot \left(\frac{\rho_l}{M_l} \mathbf{u}_l \right) + R_w = 0 \quad \text{(liquid phase)}, \tag{8}$$

where $D_{O_2}^{eff}$ and D_v^{eff} stand for the effective diffusivity of the oxygen and water vapor; ρ_l and M_l denote the density and molar weight of the water; R_w is the interfacial transfer rate of water between liquid and vapor water (see Table 1); $\mathbf{u}_l$ is the superficial velocity vector based on the total cross-sectional area of fluids and porous medium, which can be obtained from Darcy's law:

$$\mathbf{u}_l = -\frac{K k_{rl}}{\mu_l} \nabla p_l, \tag{9}$$

where k_{rl} is the relative permeability of the liquid phase, μ_l is the viscosity of the liquid water, p_l is the pressure of the liquid phase. Similarly, according to the definition of the capillary force shown in Eq. (4) and the assumption of the constant gas pressure on the cathode, we can obtain:

$$\nabla \cdot \left(-\frac{\rho_l}{M_l} \frac{K k_{rl}}{\mu_l} \sigma \cos(\theta_c) \left(\frac{\varepsilon}{K} \right)^{0.5} \nabla J(s) \right) + R_w = 0. \tag{10}$$

2.3. Mass transport in the membrane

We now consider the transport of methanol and water through the membrane. Methanol permeates the membrane as the result of the concentration gradient and electro-osmotic drag by the proton transfer. Accordingly, the flux of methanol through the membrane, N_{cross}, can be determined from:

$$N_{cross} = -D_{m,mem}^{eff} \frac{dC_{m,mem}}{dx} + n_d^m \frac{i}{F}, \tag{11}$$

Table 1
Constitutive relations and definitions

Parameters	Expressions
Capillary pressure	$p_c = p_g - p_l = \sigma \cos\theta_c (\varepsilon/K)^{0.5} J(s)$ $J(s) = \begin{cases} 1.417(1-s) - 2.120(1-s)^2 + 1.263(1-s)^3 & 0 < \theta_c < 90^\circ \\ 1.417s - 2.120s^2 + 1.263s^3 & 90^\circ < \theta_c < 180^\circ \end{cases}$
Relative permeability	$k_{rl} = s^3$ liquid $k_{rg} = (1-s)^3$ gas
Effective diffusion coefficients of species	$D_i^{eff} = D_i \varepsilon^{1.5} (1-s)^{1.5}$ i : O_2, vapor CGDL $D_i^{eff} = D_i \varepsilon^{1.5} s^{1.5}$ i : methanol AGDL
The saturation pressure of vapor	$\log_{10} p_v^{sat} = \begin{matrix} -2.1794 + 0.02953(T-273) \\ -9.1837 \times 10^{-5}(T-273)^2 \\ +1.4454 \times 107(T-273)^3 \end{matrix}$ atm
Interfacial transfer rate of water between liquid and vapor [34]	$R_w = \begin{cases} k_e \frac{\varepsilon s \rho_l}{M_{H_2O}} (y_v p_g - p_v^{sat}) & y_v p_g < p_v^{sat} \\ k_v \frac{\varepsilon(1-s) y_v}{RT} (y_v p_g - p_v^{sat}) & y_v p_g > p_v^{sat} \end{cases}$

where $D^{\text{eff}}_{\text{m,mem}}$ is the effective diffusivity of methanol in the membrane, F is the Faraday's constant (96,485 C mol^{-1}), n^{m}_{d} is the electro-osmotic drag coefficient of methanol. The transport of liquid water through the membrane is also driven by the electro-osmotic drag and concentration gradient. However, since the concentration difference of water across the membrane is rather small, the flux of water can be determined by considering the electro-osmotic drag only, i.e.:

$$N_{\text{H}_2\text{O}} = n_{\text{H}_2\text{O}} \frac{i}{F} \tag{12}$$

with $n_{\text{H}_2\text{O}}$ denoting electro-osmotic drag coefficient of water.

2.4. Heat transfer

We now consider the heat transfer process in the passive DMFC. On the anode, the heat generated by the electrochemical reaction in the ACL, is given by:

$$q_{\text{acl}} = i\left(\eta_{\text{a}} - \frac{\Delta H_{\text{a}} - \Delta G_{\text{a}}}{6F}\right), \tag{13}$$

where the first term represents the heat generation due to the activation and mass transfer overpotentials on the anode, the second term represents the entropy change of the anodic electrochemical reaction, with ΔH_{a} denoting the anodic reaction enthalpy and ΔG_{a} the Gibbs free energy.

The heat generation in the CCL, q_{ccl}, can be determined from:

$$q_{\text{ccl}} = (i + i_{\text{p}})\eta_{\text{c}} - (i + i_{\text{p}})\frac{\Delta H_{\text{c}} - \Delta G_{\text{c}}}{4F} - i_{\text{p}}\frac{\Delta H_{\text{a}} - \Delta G_{\text{a}}}{6F}, \tag{14}$$

where the first term represents the heat generation due to activation and mass transfer overpotentials and mixed potential caused by methanol crossover on the cathode, the second term accounts for the entropic loss, with ΔH_{c} denoting the cathodic reaction enthalpy and ΔG_{c} the Gibbs free energy, and the third term denotes the entropy change of methanol oxidation reaction on the cathode due to methanol crossover.

Since the fuel tank, ACC, and AGDL are assumed to be well insulated from the ambient, the heat generated within the cell is lost to the ambient from the cathode. The heat transfer process involves three components: the membrane, CGDL and CCC. Since the flow velocity in the passive DMFC is rather small, the heat transfer process through the membrane, CGDL and CCC can be modeled as a heat-conduction problem as follows:

$$\nabla \cdot (-\lambda_i \nabla T) = 0, \quad i : \text{MEM, CCC}, \tag{15a}$$

and

$$\nabla \cdot (-\lambda_i \nabla T) = h_{\text{v}} R_{\text{w}}, \quad i : \text{CGDL}, \tag{15b}$$

where λ_i is the effective thermal conductivity of each component, h_{v} is the latent heat of vaporization of liquid water, R_{w} is the water evaporation rate.

2.5. Electrochemical kinetics

On the anode, the methanol oxidation reaction is a complicated multi-step electrochemical reaction. For simplification, we assume the MOR is a first-order reaction. Thus, the current density can be determined by the simplified Tafel equation:

$$i = i^{\text{ref}}_{\text{m}} \frac{C_{\text{m,acl}} s}{C^{\text{ref}}_{\text{m}}} \exp\left(\frac{\alpha_{\text{a}} F}{RT_{\text{acl}}}\eta_{\text{a}}\right), \tag{16}$$

where $i^{\text{ref}}_{\text{m}}$ and $C^{\text{ref}}_{\text{m}}$ represent, respectively, the reference exchange current density on the anode and the reference concentration of methanol, $C_{\text{m,acl}}$ and s stand for the methanol concentration and the liquid saturation at the ACL.

On the cathode, to account for the effect of methanol crossover on the cathode overpotential, we assume that the methanol permeated from the anode completely and electrochemically reacts with the oxygen on the cathode. Based on this assumption, the internal current, i_{p}, due to the methanol oxidation on the cathode can be obtained based on the permeation flux of methanol [28]:

$$i_{\text{p}} = \frac{1}{6F} N_{\text{cross}}. \tag{17}$$

It follows from Eqs. (16) and (17) that the cathode overpotential taking account of the mixed potential can be determined from:

$$i + i_{\text{p}} = i^{\text{ref}}_{\text{O}_2} \frac{C_{\text{O}_2,\text{ccl}}(1 - s)}{C^{\text{ref}}_{\text{O}_2}} \exp\left(\frac{\alpha_{\text{c}} F}{RT_{\text{ccl}}}\eta_{\text{c}}\right), \tag{18}$$

where $i^{\text{ref}}_{\text{O}_2}$ and $C^{\text{ref}}_{\text{O}_2}$ represent, respectively, the reference exchange current density on the cathode and the reference concentration of oxygen, $C_{\text{O}_2,\text{ccl}}$ and s denote the oxygen concentration and liquid saturation at the CCL.

2.6. Boundary conditions

At the outer surface of the AGDL and CGDL, the methanol concentration, oxygen concentration and water vapor concentration are given based on the reactant supplying conditions. The internal interfacial conditions are given based on the continuity and mass/species flux balance to satisfy the general mass and species conservation of the entire cell. The boundary conditions at each interface shown in Fig. 1b are detailed in Table 2.

2.7. Cell performance

The protons and electrons produced from the MOR in the ACL transfer to the cathode through the membrane and the external circuit, respectively. The mean cell current density can be calculated by:

$$I = \frac{\int i \, \text{d}y}{l}. \tag{19}$$

Similarly, on the cathode, the mean parasitic current density generated by the cathode methanol oxidation can be determined from:

$$I_{\text{p}} = \frac{\int i_{\text{p}} \, \text{d}y}{l}. \tag{20}$$

With the methanol/oxygen concentration at the catalyst layers and the temperature distributions, and the anodic and cathodic

Table 2
Boundary conditions

	Boundary conditions
I	$C_m = C_{m,\infty}, \quad s = 0.95$
II	$\frac{dC_m}{dx} = 0, \quad \frac{ds}{dx} = 0$
III	$N_m = \frac{i}{6F} + N_{cross}, \quad -\frac{K\rho_g k_{rg}}{M_g \mu_g}\nabla p_g = \frac{i}{6F}, \quad q_{acl} = i\left(\eta_a - \frac{\Delta H_a - \Delta G_a}{nF}\right)$
IV	$N_{O_2} = \frac{i}{4F} + \frac{3}{2}N_{cross}, \quad N_{H_2O} = 2N_{cross} + n_{H_2O}\frac{i}{F} + \frac{i}{2F}, \quad q_{ccl} = (i + i_p)\eta_c - i\frac{\Delta H_c - \Delta G_c}{nF}$
V	$C_{O_2} = C_{O_2,\infty}, \quad C_v = C_{v,\infty}, \quad s = 0.05, \quad -\lambda_{cgdl}\frac{dT}{dx} = h(T - T_\infty)$
VI	$\frac{dC_{O_2}}{dx} = 0, \quad \frac{dC_v}{dx} = 0, \quad \frac{ds}{dx} = 0, \quad \lambda_{cgdl}\frac{dT}{dx} = \lambda_{ccc}\frac{dT}{dx}$
VII	$\lambda_{ccc}\frac{dT}{dy} = h(T - T_\infty)$
VIII	$-\lambda_{ccc}\frac{dT}{dx} = h(T - T_\infty)$
IX	$\frac{dC_m}{dy} = 0, \quad \frac{dC_{O_2}}{dy} = 0, \quad \frac{dC_v}{dy} = 0, \quad \frac{ds}{dy} = 0, \quad \frac{dT}{dy} = 0$
X	$\frac{dC_m}{dy} = 0, \quad \frac{dC_{O_2}}{dy} = 0, \quad \frac{dC_v}{dy} = 0, \quad \frac{ds}{dy} = 0, \quad \frac{dT}{dy} = 0$

overpotentials obtained from the equations presented above, we can assess the cell performance based on:

$$V_{cell} = E_{cell} - \eta_a - \eta_c - I\frac{\delta}{\kappa} - IR_{contact}, \tag{21}$$

where E_{cell} is the thermodynamic equilibrium potentials of the fuel cell and is a function of temperature and pressure, $R_{contact}$ is the contact resistance of the fuel cell. The thermodynamic equilibrium potentials of the fuel cell can be calculated by:

$$E_{cell} = E^0_{cell} + \Delta T\left(\frac{\partial E}{\partial T}\right), \tag{22}$$

where E^0_{cell} is the open circuit voltage at $T = 298$ K and $(\partial E/\partial T)$ represents the change rate of electromotive force of -1.4×10^{-4} V K^{-1} [49].

3. Results and discussion

Using a self-written code based on the *SIMPLE* algorithm, all the variables are iteratively solved based on the physicochemical properties given in Table 3 until the pre-set convergent criterions are met. With this model, the effects of several parameters including the methanol concentration and collector design on cell performance were investigated. Details are presented below.

3.1. Effect of methanol concentration

Fig. 2 shows the polarization curves when the fuel cell operates with 1–4 M methanol solutions, respectively. It can be seen from this figure that the cell performance upgrades progressively with an increase in methanol concentration. The increased cell performance as the result of increasing methanol concentration can be explained as follows. Firstly, the mass transfer rate of

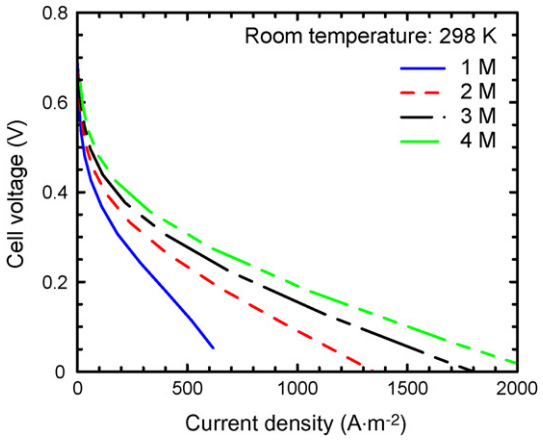

Fig. 2. Effect of the methanol concentration on the performance of the passive DMFC.

methanol at the anode increases with methanol concentration, reducing the voltage loss on the anode due to the mass transfer polarization and thereby tending to yield better cell performance. Secondly, Fig. 3 also shows that the rate of methanol crossover increases with methanol concentration. The increased rate of methanol crossover results in a larger mixed potential, which tends to reduce the cell voltage. Meanwhile, it is also seen that the rate of methanol crossover decreases with the current density as a result of the reduced methanol concentration at the anode electrode/membrane interface. Thirdly, the increased rate of methanol crossover as the result of higher methanol concentration will also lead to a higher rate of methanol oxidation on the cathode, which in turn results in a higher heat generation rate. As a result, the cell operating temperature virtually increases with methanol concentration, as evidenced from Fig. 4, which shows the variation in the temperature at the ACL with current density for different methanol concentrations. In particular, it is seen that the temperature difference between different methanol-concentration operations at low current densities and open circuit condition (OCC) is much larger than that at middle and high current densities. This is because the methanol crossover is more serious at low current densities and OCC, leading to a higher heat generation rate and thereby larger temperature difference. The increased operating temperature fasters

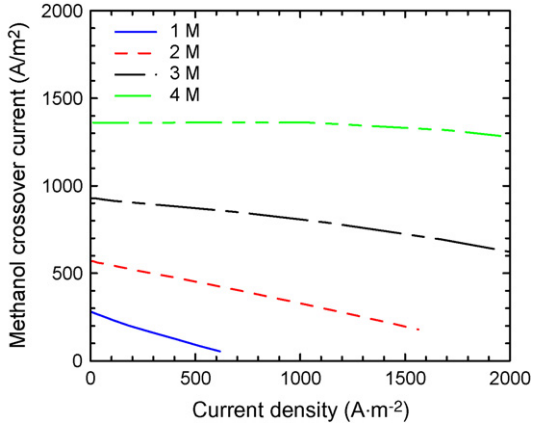

Fig. 3. Variations in the methanol crossover current with current density for different methanol concentrations.

Table 3
Physicochemical properties

Parameter, symbol (unit)	Value	Refs.
Liquid methanol enthalpy of formation, ΔH_m (J mol^{-1})	-238.66×10^3	
Liquid water enthalpy of formation, ΔH_w (J mol^{-1})	-285.83×10^3	
Carbon dioxide enthalpy of formation, ΔH_{CO_2} (J mol^{-1})	-393.51×10^3	
Liquid methanol Gibbs free energy, ΔG_m (J mol^{-1})	-166.27×10^3	
Liquid water Gibbs free energy, ΔG_w (J mol^{-1})	-237.08×10^3	
Carbon dioxide Gibbs free energy, ΔG_{CO_2} (J mol^{-1})	-394×10^3	
Liquid methanol specific heat capacity, c_m (J mol^{-1} K^{-1})	80.96	
Liquid water specific heat capacity, c_w (J mol^{-1} K^{-1})	75.24	
Carbon dioxide specific heat capacity, c_{CO_2} (J mol^{-1} K^{-1})	36.9	
Oxygen specific heat capacity, C_{O_2} (J mol^{-1} K^{-1})	39.44	
Evaporation heat of water, h_v (J mol^{-1})	44.86×10^3	
Pressure of air in cathode, P_g (Pa)	1×10^5	
Thickness of ACC and CCC, l_{ccc} (m)	0.0005	
Thickness of AGDL and CGDL, l_{gdl} (m)	0.0003	[50]
Electro-osmotic drag coefficient of water, n_{H_2O}	$2.9 \exp(1029/(1/333 - 1/T))$	[23]
Electro-osmotic drag coefficient of methanol, n_d^m	$x_m \times n_{H_2O}$	[28]
Proton conductivity in membrane, κ (1 Ω^{-1} m^{-1})	$7.3 \exp(1268(1/298 - 1/T))$	[14]
Porosity of AGDL and CGDL, ε	0.6	[33]
Permeability in AGDL and CGDL, K (m^2)	1.2×10^{-12}	[34]
Thermal conductivity of membrane, λ_{mem} (W m^{-1} K^{-1})	0.21	[24]
Thermal conductivity of CGDL, λ_{cgdl} (W m^{-1} K^{-1})	1.6	[24]
Thermal conductivity of CCC, λ_{ccc} (W m^{-1} K^{-1})	16	[24]
Heat transfer coefficient, h (W m^{-1} K^{-1})	20	[42]
Diffusion coefficient of methanol in membrane, $D_{m,mem}^{eff}$ (m^2 s^{-1})	$4.9 \times 10^{-10} \exp(2436(1/333 - 1/T))$	[14]
Diffusivity of methanol, D_m (m^2 s^{-1})	$2.8 \times 10^{-9} \exp(2436(1/333 - 1/T))$	[14]
Diffusivity of oxygen, D_{O_2} (m^2 s^{-1})	$0.1775 \times 10^{-4} \times (T/273.15)^{1.823}$	[33]
Diffusivity of water vapor, D_v (m^2 s^{-1})	$0.256 \times 10^{-4} \times (T/273.15)^{2.334}$	[33]
Density of gas phase, ρ_g (kg m^{-3})	1.98	
Density of liquid phase, ρ_l (kg m^{-3})	1×10^3	
Viscosity of gas phase, μ_g (kg m^{-1} s^{-1})	14.96×10^{-6}	
Viscosity of liquid phase, μ_l (kg m^{-1} s^{-1})	0.9×10^{-3}	
Surface tension, σ (N m^{-1})	0.0625	
Transfer coefficient of anode, α_a	0.35	[24]
Transfer coefficient of anode, α_c	0.8	[24]
Reference concentration of methanol, C_m^{ref} (mol m^{-3})	4×10^3	[24]
Reference concentration of oxygen, $C_{O_2}^{ref}$ (mol m^{-3})	$0.21 \times P_g/RT$	
Evaporation rate constant, k_e (1 atm^{-1} s^{-1})	1	[33]
Condensation rate constant, k_c (1 s^{-1})	100	[33]
Reference exchange current density on anode, i_m^{ref} (A m^{-2})	$94.25 \exp(35570/R^*(1/353 - 1/T))$	[28]
Reference exchange current density on cathode, $i_{O_2}^{ref}$ (A m^{-2})	$0.04222 \exp(73200/R^*(1/353 - 1/T))$	[28]
Contact resistance, $R_{contact}$ (Ω cm^2)	0.8	[23]

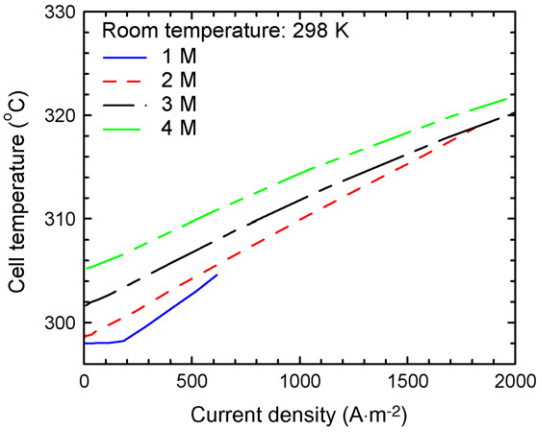

Fig. 4. Variations in the operating temperature at the ACL with current density for different methanol concentrations.

the electrochemical kinetics on both the anode and cathode, producing a higher voltage at a given current density. Therefore, the improved performance with increasing methanol concentration shown in Fig. 2 can be attributed to the increased cell operating temperature and the increased mass transfer rate of methanol, although the mixed potential on the cathode also increases with methanol concentration. The variation in the cell performance with methanol concentration is consistent with that reported elsewhere [24]. It is also noted from Fig. 4 that for each methanol concentration, the temperature at the ACL increases with current density. This is because the heat generation rate due to the kinetic and mass transfer polarization increases with current density.

3.2. Effect of current-collector open ratio

The effect of the current-collector open ratio was studied by equipping the DMFC with identical current collectors at both

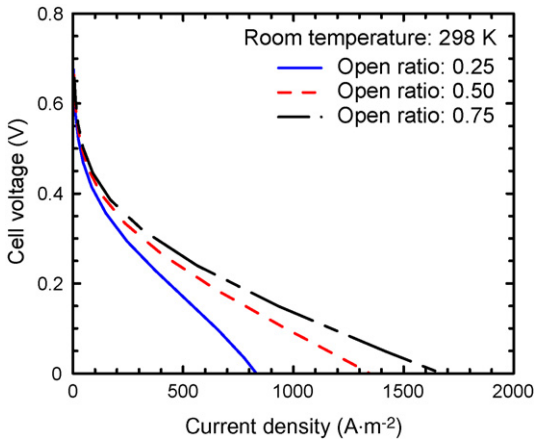

Fig. 5. Effect of the open ratio on the performance of the passive DMFC.

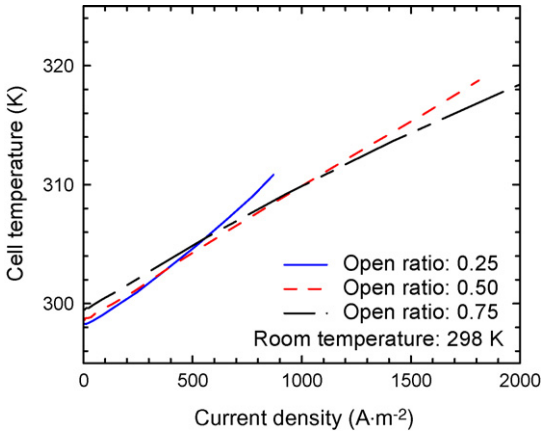

Fig. 6. Variations in the operating temperature at the ACL with current density for different open ratios.

the anode and cathode. The open ratio was changed by fixing the sum of channel and rib width at 2.0 mm. Fig. 5 shows that the cell performance increases with the open ratio, particularly at high current densities. The improved cell performance as the result of increasing the open ratio can be primarily attributed to the enhanced mass transfer rates of both methanol and oxygen. The reasons leading to the increased mass transfer rates are as follows. Firstly, the specific area of mass transfer increases with the open ratio, yielding higher mass transfer rates of both methanol and oxygen. Secondly, the rib width decreases with the open ratio, providing a shorter distance of mass transfer from the channel region to the rib region in the GDL and thereby resulting in the higher methanol and oxygen concentration under the ribs. Thirdly, the gas CO_2 on the anode and liquid water on the cathode are more easily to be removed from the rib region to the outside as the open ratio increases. Subsequently, more active sites can be used for the electrochemical reaction in the catalyst layer, leading to the improved cell performance.

The variations in the cell temperature at the ACL with the current density for different open ratios are shown in Fig. 6. For each open ratio, the cell temperature increases with the cur-

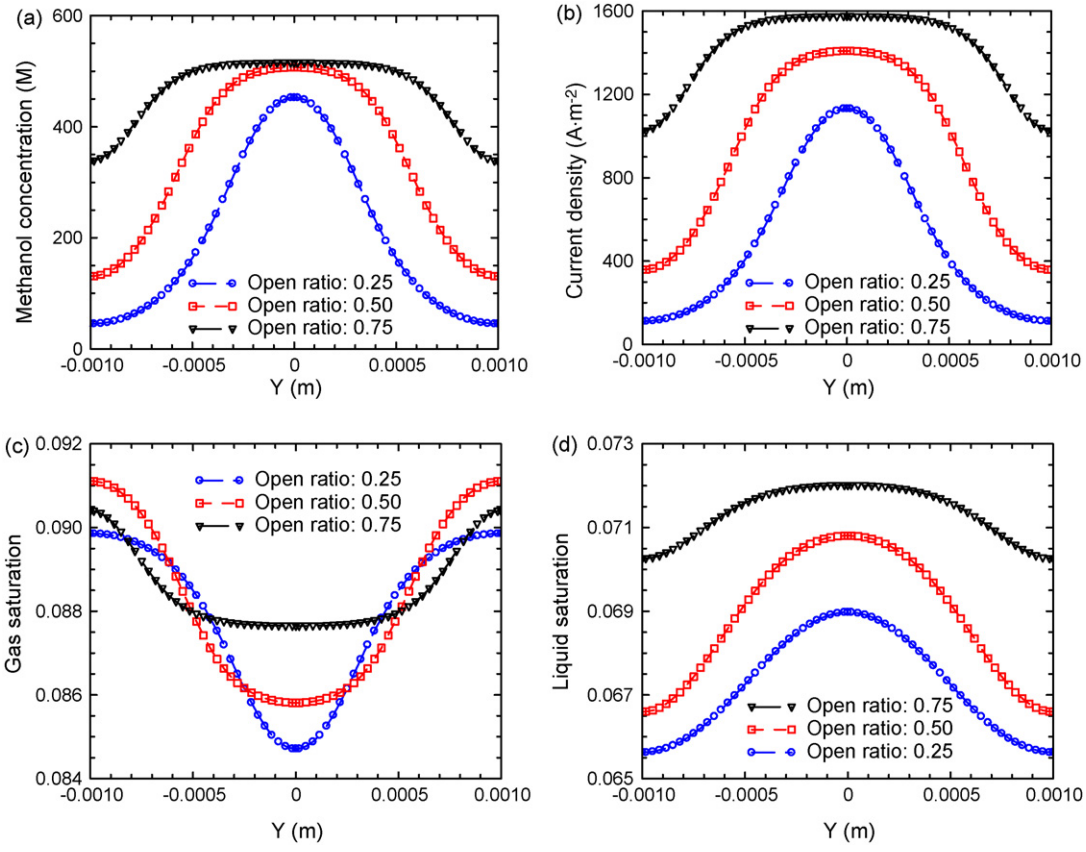

Fig. 7. Distribution of (a) methanol concentration at the ACL, (b) current density, (c) gas saturation at the ACL, (d) liquid saturation at the CCL with different open ratios.

rent density, as the heat generation rate due to the kinetic and mass transfer polarization increases with the current density. It is interesting to notice that at low current densities, the larger open ratio yields a slightly higher cell operating temperature than does the smaller one, but at high current densities the trend reverses. This is because the larger open ratio yields a higher rate of methanol crossover at low current densities, resulting in a higher mixed potential on the cathode, which in turn causes a higher heat generation rate on the cathode. As a result, the larger open ratio yields a slightly higher cell temperature at low current densities. As the current density increases, the overpotential due to the mass transfer becomes more dominant. The increased mass transfer loss with the smaller open ratio produces more heat at high current densities, leading to a higher cell temperature. Moreover, the increased rib region as the result of reduction in the open ratio also increases the heat transfer resistance from the cell to the ambient, reducing the heat loss. This also contributes to the higher cell temperature for the smaller open ratio at high current densities. It should be pointed that since the cell temperature change with the open ratio is rather small, it has little effect on the cell performance. Therefore, the improved cell performance as the result of increasing the open ratio shown in Fig. 5 can be mainly attributed to the increased rates of methanol transfer on the anode and oxygen transfer on the cathode.

Fig. 7 shows the distributions of methanol concentration at the ACL, current density, gas saturation at the ACL, and liquid saturation at the CCL for different open ratios at a given anode overpotential of 0.5 V. It is seen from Fig. 7a that a more uniform distribution of methanol concentration is achieved with increasing the open ratio as the result of the enhanced mass transfer mentioned earlier, which in turn leads to higher and more uniform distribution of current density, as shown in Fig. 7b. These results further confirm that the improved cell performance shown in Fig. 5 is primarily due to the enhanced mass transfer rates resulting from the large open ratio. Meanwhile, a higher current density produces more gas CO_2 on the anode and liquid water on the cathode. As a result, the larger open ratio yields higher gas saturation at the ACL and liquid saturation at CCL, as shown in Fig. 7c and d. It is also found that since the gas CO_2 is difficult to transport from the rib region to the outside due to the larger mass transfer resistance, leading to higher gas saturation under the rib. However, this is not the case for the liquid saturation at the CCL. The liquid saturation under the rib is lower than that under the channel region because of the lower water generation rate.

The cell temperature distributions in the x and y directions for different open ratios at a given anode overpotential of 0.5 V are presented in Fig. 8. It is seen from this figure that a larger open ratio exhibits a higher cell temperature because a higher current density leads to a higher heat generation rate. It is interesting to notice that the variation trend in the cell temperature shown in Fig. 8a is similar to the current density distribution shown in Fig. 7b. This is because the heat generation rate is proportional to the current density. The higher current density at the channel region results in the higher heat generation rate and thus higher cell temperature. Since the heat is generated at the ACL and CCL and released from the cathode to the ambient,

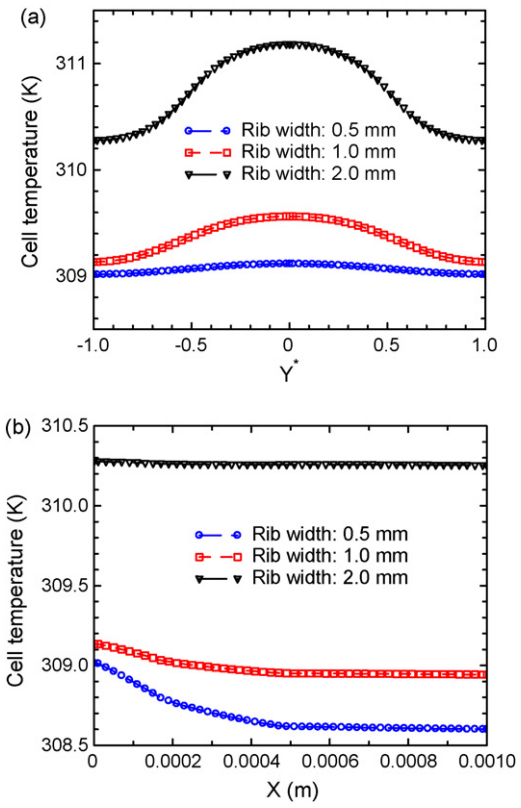

Fig. 8. Distribution of (a) cell temperature in y direction, (b) cell temperature in x direction with different open ratios.

the cell temperature decreases along the x direction, as shown in Fig. 8b. Particularly, the larger open ratio shows a little higher temperature gradient in the cell as the result of the increased heat generation rate. However, because the thickness of the membrane, CGDL and CCC is relatively small, the overall variation of the cell temperature in the cell is small.

3.3. Effect of the channel and rib width

We now turn our attention to the effect of the channel and rib width. The simulations were performed by keeping the ratio of

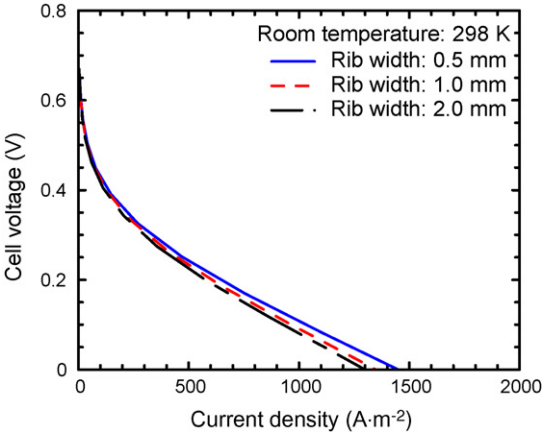

Fig. 9. Effect of the channel and rib width on the performance of the passive DMFC.

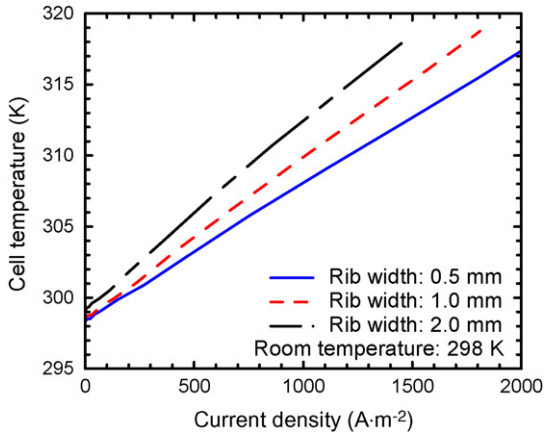

Fig. 10. Variations in the operating temperature at the ACL with current density for different channel and rib width.

the channel width to rib width at 1:1. Hence, hereafter a specified rib width also means the same size in the channel width. Also note that the both current collectors on the anode and cathode are identical. Figs. 9 and 10 show the cell performance and variation in the cell temperature at the ACL with the current density at 2.0 M methanol operation, respectively. It is seen from Fig. 9 that the cell performance decreases with the rib width. This is because the distance of mass transfer from the channel region to the rib region increases with the rib width, leading to a higher mass transfer resistance and thereby a lower methanol and oxygen concentration under the ribs. Moreover, the larger rib width also exacerbates the removal of the gas CO_2 and liquid water, which further reduces the methanol concentration at the ACL and oxygen concentration at the CCL. As a result, the cell performance decreases with the rib width. In the meantime, at a given current density, the overpotential increases with the rib width as the result of the increased mass transfer resistance, resulting in a higher heat generation rate and thereby a higher cell temperature, as shown in Fig. 10. Particularly, because the effect of the mass transfer becomes more significant at high current densities, more heat due to the mass transfer polarization is generated. Therefore, the temperature difference between different rib widths increases with the current density. However, although the cell temperature is higher with the larger rib width, the cell performance is still lower. This fact indicates that the effect of the increased mass transfer as the result of decreasing the rib width is more important than the effect of the increased temperature on the cell performance. Hence, the improved cell performance with decreasing the rib width is mainly attributed to the increased mass transfer rate on the anode and cathode.

Fig. 11 shows the distributions of methanol concentration at the ACL, current density, gas saturation at the ACL and liquid saturation at the CCL for different rib widths at a given anode overpotential of 0.5 V. It should be noted that the rib width is normalized to the total width of the channel and rib for the purpose of comparison. It is seen that the smaller rib width shows a higher methanol concentration and more uniform distribution.

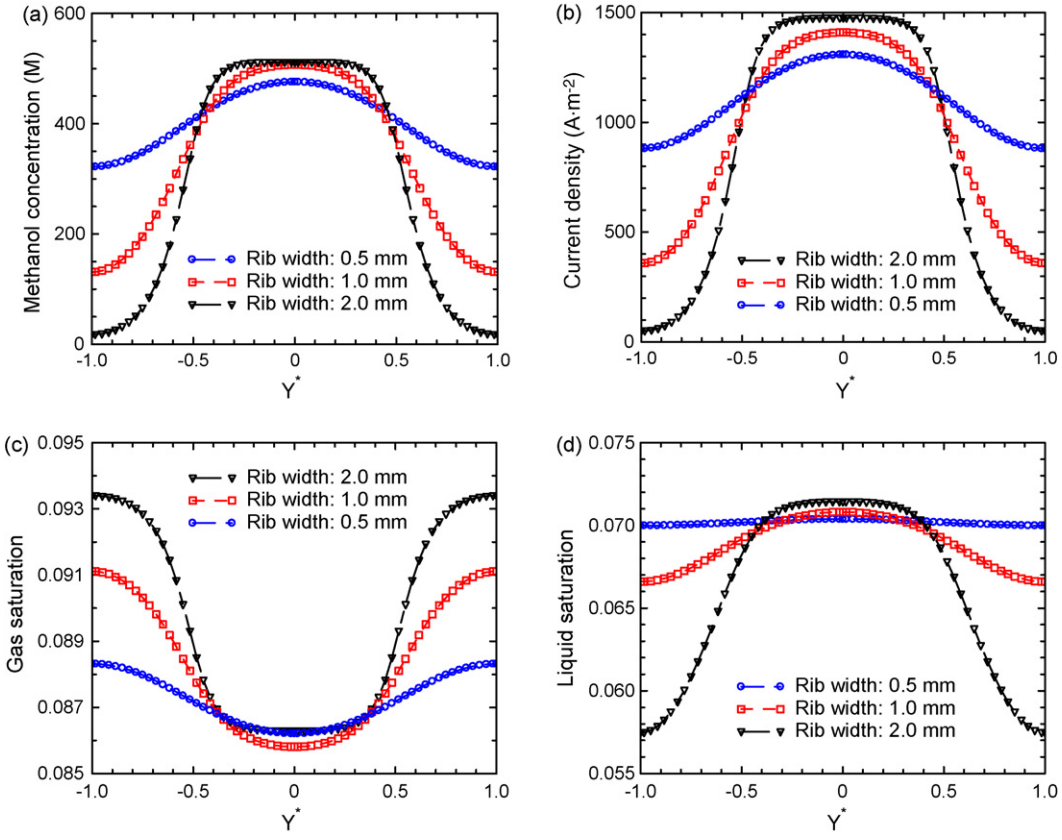

Fig. 11. Distribution of (a) methanol concentration at the ACL, (b) current density, (c) gas saturation at the ACL, (d) liquid saturation at the CCL with different channel and rib width.

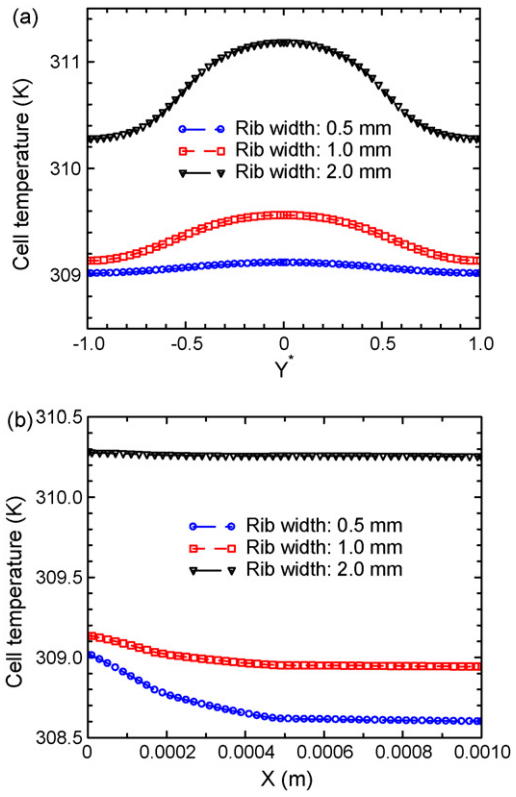

Fig. 12. Distribution of (a) cell temperature in y direction, (b) cell temperature in x direction with different channel and rib width.

This is because the smaller rib width leads to a shorter distance of mass transfer and thereby a lower overall mass transfer resistance. The lowered overall mass transfer resistance leads to a higher methanol and oxygen concentration to produce a higher and more uniform current density, as shown in Fig. 11b. This is also the reason why the smaller rib width yields better cell performance shown in Fig. 9. As mentioned in the above subsection, a larger rib width leads to a larger mass transfer resistance of the gas CO_2 from the rib region to the outside. Hence, the gas saturation under the rib region is higher, as shown in Fig. 11c. Additionally, although the generation rate of the gas CO_2 is larger at the ACL for the smaller rib width because of the larger current density, the gas saturation at the ACL is still lower than that of the larger rib width as the result of the lowered mass transfer resistance. On the contrary to the anode, the smaller rib width yields higher liquid saturation at the CCL because of the higher water generation rate resulting from the higher current density, as shown in Fig. 11d. Moreover, the liquid saturation distribution is more uniform for the smaller rib width as a result of the lowered mass transfer resistance.

The temperature distributions in the x and y directions for different rib widths at a given anode overpotential of 0.5 V are presented in Fig. 12. From this figure, it can be seen that the larger rib width exhibits a higher cell temperature. This can be attributed to the lower water evaporation rate resulting from the larger rib width. Moreover, the current density at the channel region is higher, resulting in a higher heat generation rate and thereby a higher cell temperature at the channel region. In addition, the cell temperature decreases from the anode to the outer surface of the CCC because all the heat is released to the ambient from the cathode. It is interesting to notice that although the cell temperature is higher with the larger rib width, the cell performance is still lower. This fact reveals that the mass transfer is a predominant factor that affects the cell performance when the rib width is varied.

4. Concluding remarks

A two-dimensional, two-phase mass transport model for a passive DMFC with the heat transfer effect has been developed based on the unsaturated flow theory in porous media. A computer code was then developed for solving the equations that govern the interrelated heat and mass transport, along with the electrochemical reactions occurring in the passive DMFC. The effects of the open ratio and channel and rib width of the current collectors and methanol concentration on cell performance were investigated. It is revealed that the improved performance as the result of higher methanol concentrations is due primarily to the increased cell operating temperature resulting from the exothermic reaction between permeated methanol and oxygen on the cathode and increased mass transfer rate of methanol. It is also found that the cell performance improves with increasing the open ratio, which results in the improved mass transport of both methanol and oxygen, although the cell operating temperature decreases slightly with the open ratio. Finally, the numerical results show that the cell performance degrades with increasing the rib width (or channel width), which is attributed mainly to the increased mass transfer resistance at the both anode and cathode, although the cell operating temperature increases with the rib width.

Acknowledgement

The work described in this paper was fully supported by a grant from the Research Grants Council of the Hong Kong Special Administrative Region, China (Project No. 622305).

References

[1] C.K. Dyer, J. Power Sources 106 (2002) 31.
[2] J. Prabhuram, T.S. Zhao, C.W. Wong, et al., J. Power Sources 134 (2004) 1.
[3] H. Yang, T.S. Zhao, Q. Ye, J. Power Sources 139 (2005) 79.
[4] C.Y. Chen, P. Yang, J. Power Sources 123 (2003) 37–42.
[5] J.G. Liu, G.G. Sun, F.L. Zhao, et al., J. Power Sources 133 (2004) 175.
[6] D. Kim, E.A. Cho, S.A. Hong, et al., J. Power Sources 130 (2004) 172.
[7] T. Shimizu, T. Momma, M. Mohamedi, et al., J. Power Sources 137 (2004) 277.
[8] M.A. Abdelkareem, N. Nakagawa, J. Power Sources 162 (2006) 114.
[9] R. Chen, T.S. Zhao, J.G. Liu, J. Power Sources 157 (2006) 351.
[10] R. Chen, T.S. Zhao, Electrochem. Commun. 9 (2007) 718.
[11] R. Chen, T.S. Zhao, Electrochim. Acta 52 (2007) 4317.
[12] R. Chen, T.S. Zhao, J. Power Sources 167 (2007) 455.
[13] P. Argyropoulos, K. Scott, A.K. Shukla, et al., J. Power sources 123 (2003) 190.
[14] K. Scott, W.M. Taama, J. Cruichshank, J. Power Sources 65 (1997) 159.
[15] B.L. Garcia, V.A. Sethuraman, J.W. Weidner, et al., J. Fuel Cell Sci. Technol. 1 (2004) 43.

[16] K.T. Jeng, C.W. Chen, J. Power Sources 112 (2002) 367.
[17] A.A. Kulikovsky, J. Appl. Electrochem. 30 (2000) 1005.
[18] A.A. Kulikovsky, Electrochem. Commun. 6 (2004) 1259.
[19] J.P. Meyers, J. Newman, J. Electrochem. Soc. 149 (2002) A710.
[20] J.P. Meyers, J. Newman, J. Electrochem. Soc. 149 (2002) A718.
[21] E. Birgersson, J. Nordlund, H. Ekstrom, et al., J. Electrochem. Soc. 150 (2003) A1368.
[22] J. Nordlund, G. Lindbergh, J. Electrochem. Soc. 149 (2002) A1107.
[23] H. Guo, C.F. Ma, Electrochem. Commun. 6 (2004) 306.
[24] R. Chen, T.S. Zhao, J. Power Sources 152 (2005) 122.
[25] C.H. Chen, T.K. Yeh, J. Power Sources 160 (2006) 1131.
[26] Q. Ye, T.S. Zhao, C. Xu, Electrochim. Acta 51 (2006) 5420.
[27] G. Murgia, L. Pisani, A.K. Shula, et al., J. Electrochem. Soc. 150 (2003) A1231.
[28] Z.H. Wang, C.Y. Wang, J. Electrochem. Soc. 150 (2003) A508.
[29] E. Birgersson, J. Nordlund, M. Vynnycky, et al., J. Electrochem. Soc. 151 (2004) A2157.
[30] J. Divisek, J. Fuhrmann, K. Gartner, et al., J. Electrochem. Soc 150 (2003) A811.
[31] D. Natarajan, T.V. Nguyen, J. Electrochem. Soc. 148 (2001) A1324.
[32] G.Y. Lin, W.S. He, T.V. Nguyen, J. Electrochem. Soc. 151 (2004) A1999.
[33] G.Y. Lin, T.V. Nguyen, J. Electrochem. Soc. 153 (2006) A372.
[34] W.H. He, J.S. Yi, T.V. Nguyen, AIChE J. 46 (2000) 2053.
[35] W.W. Yang, T.S. Zhao, Electrochim. Acta 52 (2007) 6125.
[36] B.P.M. Rajani, A.K. Kolar, J. Power Sources 164 (2007) 210.
[37] S.U. Jeong, E.A. Cho, H.J. Kim, et al., J. Power Sources 159 (2006) 1089.
[38] S. Litster, J.G. Pharoah, G. McLean, et al., J. Power Sources 156 (2006) 334.
[39] R. O'Hayre, T. Fabian, S. Litster, et al., J. Power Sources 167 (2007) 118.
[40] J.J. Hwang, S.D. Wu, R.G. Pen, et al., J. Power Sources 160 (2006) 18.
[41] S. Litster, N. Djilali, Electrochim. Acta 52 (2007) 3849.
[42] C. Ziegler, A. Schmitz, M. Tranitz, et al., J. Electrochem. Soc. 151 (2004) A2028.
[43] D. Chu, R.Z. Jiang, J. Power Sources 83 (1999) 128.
[44] J.J. Hwang, J. Electrochem. Soc. 153 (2006) A1584.
[45] W. Ying, Y.J. Sohn, W.Y. Lee, et al., J. Power Sources 145 (2005) 563.
[46] W. Ying, T.H. Yang, W.Y. Lee, et al., J. Power Sources 145 (2005) 572.
[47] J.J. Hwang, S.D. Wu, L.K. Lai, et al., J. Power Sources 161 (2006) 240.
[48] J. Rice, A. Faghri, Int. J. Heat Mass Transfer 49 (2006) 4804.
[49] K. Scott, P. Argyropoulos, K. Sundmacher, J. Electroanal. Chem. 477 (1999) 97.
[50] K. Scott, W.M. Taama, S. Kramer, et al., Electrochim. Acta 45 (1999) 945.